Abnormal magnetic phase transition in mixed-phase (110)oriented FeRh films on Al₂O₃ substrates via the anomalous Nernst effect

Jae Won Choi^{1,†}, Chanho Park^{1,†}, Gil-Sung Kim¹, Jung-Min Cho¹, No-Won Park¹, Yun-Ho Kim¹, Min Young Jung¹, Seo Hyoung Chang¹, Md Sabbir Akhanda², Bellave Shivaram³, Steven P. Bennett⁴, Mona Zebarjadi^{2,5}, and Sang-Kwon Lee^{1,*}

FeRh exhibits a first order anti-ferromagnetic (AFM) to ferromagnetic (FM) phase transition due to the magnetic moment that is induced in Rh atoms above a Curie temperature (T_c). By measuring the anomalous Nernst effect (ANE), which is a result of a spontaneous drop in the transverse voltage driven by the temperature gradient in a magnetic material, over a temperature range of 100-350 K, we observed the ANE thermopower in (110)-oriented FeRh films on Al_2O_3 substrates, with similar magnetic transport behaviors observed for in-plane magnetization (IM) and out-of-plane magnetization (PM) configurations. The temperature-dependent magnetization—magnetic field strength (M-H) curves revealed that the ANE voltage was proportional to the magnetization of the material, but additional features magnetic textures not shown in the M-H curves remained intractable. In particular, a sign reversal occurred for the ANE thermopower signal near zero field in the mixed-magnetic-phase films at low temperatures, which was attributed to the diamagnetic properties of the Al_2O_3 substrate. Finite element method simulations associated with the Heisenberg spin model and Landau—Lifshitz—Gilbert equation strongly supported the abnormal heat transport behavior from the Al_2O_3 substrate during the experimentally observed magnetic phase transition for the IM and PM configurations. Our results demonstrate that FeRh films on an Al_2O_3 substrate exhibit unusual behavior compared to other ferromagnetic materials, indicating their potential for use in novel applications associated with practical spintronics device design, neuromorphic computing, and magnetic memory.

¹Department of Physics, Chung-Ang University, Seoul 06974, Republic of Korea

²Department of Electrical and Computer Engineering, University of Virginia, Charlottesville, VA 22904, USA

³Department of Physics, University of Virginia, Charlottesville, VA 22904, USA

⁴Materials Science and Technology Division, U.S. Naval Research Laboratory, Washington, DC 20375, USA

⁵Department of Materials Science and Engineering, University of Virginia, Charlottesville, VA 22904, USA

^{*}Corresponding author. Email: sangkwonlee@cau.ac.kr

[†]These authors contributed equally to this work

1. Introduction

The thermopower of magnetic materials, in which the magnetic order couples with thermal input, has gained significant research interest for potential use in spintronics applications, where a material can be heated or cooled by controlling the magnetic field. [1-4] In this field of research, thin-film materials that exhibit magnetic phase transitions are widely employed to gain insights into the development of new device applications. For example, iron rhodium (FeRh) has been employed as a key material for the observation of magnetic phase transitions in response to changes in temperature^[5-7] because it experiences a phase transition at two points: an anti-ferromagnetic (AFM) to ferromagnetic (FM) phase transition at the first Curie temperature (T_{C1}) and an FM to paramagnetic phase transition at the second Curie temperature (T_{C2}) . In addition, by controlling the magnetic phase transition temperature via strain/tensile effects induced by epitaxial growth on different substrates or introducing defects to metamagnetic materials, FeRh-based applications using direct write-in device techniques or martensitic approaches have been reported.^[8-11] Enhancing spin-mixing conductance by creating homojunctions using FeRh films with different magnetic states has also gained considerable interest for spintronics devices, even though conventional FeRh/nonmagnetic metal interfaces are known to have a low spin transmission efficiency. [12, 13] Due to the wide range of potential applications for FeRh, the mechanisms involved in the generation of heat-assisted thermoelectric power in materials with thermally driven magnetic phase transitions have received significant research attention.^[14] One of the most widely studied mechanisms is the Nernst effect, which is a thermoelectric analogue of the Hall effect^[1] in which magnetic spin and charge are coupled with heat transfer. Of particular interest is the anomalous Nernst effect (ANE), which focuses on the Nernst charge current generated solely by the internal magnetic field, which is associated with the magnetization \vec{M} of the material. The ANE can generally be expressed as the generation of a charge current from a temperature gradient and a magnetic field as follows:

$$\vec{E}_{ANE} \sim \vec{M} \times \nabla T, \tag{1}$$

where \vec{E}_{ANE} and ∇T are the electric field induced by the Nernst effect and the thermal temperature gradient across the material, respectively. In the Nernst effect, the change in the charge current of the system can be replaced by ∇T because both the Hall and Nernst effects allow the charge carriers to move in a drift-diffusion manner. For materials in an AFM state, the net \vec{M} can take various values depending on its collinear/non-collinear state coupled with the external field, leading to different thermopower signals in Nernst measurements compared with their purely FM counterparts. Consequently, metamagnetic materials that can adopt an FM or AFM state depending on the temperature (e.g., FeRh) have multiple features related to the ANE.

Recent studies on the ANE in FeRh grown on MgO substrates using magnetron sputtering have found that, at low temperatures, the magnitude of the saturation ANE signal decreases due to vanishing net magnetization in an AFM state.^[15, 16] However, the unusual characteristics observed for the low-temperature ANE in FeRh have yet to be explained. In particular, the physics underlying the thermally driven magnetic phase transition of FeRh films in both the in-plane magnetic field (IM) and out-of-plane magnetic field (PM) directions need to be understood in order to meet practical application demands, but this remains challenging. This is of crucial interest because the IM configuration can lead to the generation of the spin Seebeck effect when a detector metal is deposited on the magnetic material.^[16]

In the present study, we investigated the ANE thermopower within a temperature range of 100–350 K in (110)-oriented FeRh films grown on an Al₂O₃ substrate with an IM or PM configuration. We observed a reversal of the sign of the ANE signal around zero field in the mixed magnetic transition phase at low temperatures in both magnetic configurations. This abnormal behavior in the temperature-dependent ANE thermopower of (110)-oriented FeRh on Al₂O₃ can be explained by the diamagnetic properties of the substrate. We also verified the abnormally ordered phase of spins under different

temperature regimes using finite element method (FEM) simulations associated with the Heisenberg spin model and the Landau–Lifshitz–Gilbert (LLG) equation.

2. Results

2.1. Material Characterization of (110)-oriented FeRh Thin Film

FeRh thin films were grown on c-plane Al₂O₃ (0001) substrates using DC magnetron sputtering. The crystallographic orientation and crystalline quality of the FeRh films were assessed using high-resolution X-ray diffraction (HR-XRD, Bruker D8 Discover) with Cu $K\alpha_1$ radiation. Figure 1a presents a θ –2 θ scan of an as-grown FeRh thin film on Al₂O₃ (0001). In addition to the (000l) peaks of the c-plane Al₂O₃ substrate, two additional peaks were observed at 42.63 and 93.32°, corresponding to the (110) and (220) planes of B₂-ordered FeRh (JCPDS no. 25-1408). The lattice constants along the (110) and (220) planes were determined to be ~0.211 and ~0.106 nm, respectively, which were consistent with the reported values for B₂-ordered FeRh crystals. [17-19] This indicates that the FeRh thin film on the c-plane Al₂O₃ substrate was oriented along the [110] direction.

To determine the crystalline quality of the FeRh film, a 2θ -fixed ω -rocking curve scan of the (110) XRD peak was taken (Figure 1b). The full width at half maximum of the (110) peak was \sim 0.87°, illustrating the good crystalline quality of the FeRh film. [20] The crystallographic characteristics of the (110)-oriented FeRh thin film on the c-plane Al_2O_3 (0001) substrate were also investigated using high-resolution transmission electron microscopy (HR-TEM) and scanning TEM (STEM). Figure 1c presents cross-sectional HR-TEM images of an FeRh thin film, indicating the formation of a uniform FeRh layer with a thickness of \sim 25 nm on the c-plane Al_2O_3 (0001) substrate. An enlarged HR-TEM image and corresponding fast Fourier transform (FFT) patterns (Figures 1d–f) revealed a clean and atomically sharp interface between the (110)-oriented FeRh and (0001)-oriented Al_2O_3 , which was consistent with the

HR-XRD observations (Figures 1a and b). Figures 1g–i display atomic-resolution annual dark-field (ADF) STEM images of the FeRh/Al₂O₃, FeRh, and Al₂O₃ regions, respectively, along the $[\overline{1}\overline{1}20]$ zone axis of Al₂O₃. They reveal that the (110) plane of FeRh parallels the (0001) plane of Al₂O₃.

To determine the atomic distribution of the FeRh crystal lattice, ADF-STEM images were obtained by tilting the observed FeRh lamella (Figs. 1g and h) to the [011] zone axis. As shown in Figures 1j and k, the FeRh thin film had a high crystallinity with B₂-ordered FeRh crystals, in which the 1:1 Fe and Rh atoms are periodically arranged in the crystal lattice along the (100) direction. The lattice parameters along the $(0\overline{1}1)$ and (100) planes were determined to be ~ 0.22 and ~ 0.31 nm, which closely matched previously reported values. [19,21,22] Figures 11–n present an atomic-resolution annual bright-field (ABF)-STEM image of the ~25-nm-thick FeRh thin film and corresponding elemental mappings of Fe (K-line, purple) and Rh (L-line, green), respectively, showing a uniform elemental distribution. The chemical composition of the FeRh thin film was also analyzed using X-ray photoelectron spectroscopy (XPS). Figure 10 presents the representative Fe 2p and Rh 3d core levels with doublet peaks ~723.6 and ~710.3 eV for Fe $2p_{1/2}$ and $2p_{3/2}$, and ~ 311.7 and ~ 307.1 eV for Rh $3d_{3/2}$ and $3d_{5/2}$, respectively. Furthermore, the deconvoluted Fe $2p_{3/2}$ spectrum exhibited metallic Fe⁰ bonded with Rh⁰ at ~707.6 eV. The peaks located at ~710.2 and ~712.4 eV were assigned to Fe²⁺ and Fe³⁺, respectively, originating from the oxidation of the film surface.^[23] By calculating the relative peak area ratio between the Fe 2p_{3/2} and Rh 3d_{5/2} peaks, (See Figure S8 in Supporting Information Note 6) the average atomic percentages of Fe and Rh are determined to be 48.68% and 51.32%, respectively. It indicates that our FeRh film is assigned to be the (110)-oriented B₂-phase $Fe_{1-x}Rh_x$ (x=0.48-0.52).

2.2. Anomalous Nernst Effect of FeRh Films in IM and PM Configurations

ANE measurements in both the IM and PM configurations were taken using a physical properties measurement system (PPMS). Figure 2a presents the schematics of the ANE measurement module, which consisted of a copper puck at the bottom and an aluminum nitride (AIN) plate on which the sample was mounted using acryl screws. Temperature gradient ∇T was produced using a heater installed at the upper end of the AlN plate, and this gradient was measured using E-type thermocouples. Figure 2a displays the PM configuration, in which ∇T was applied in-plane to the sample, while the magnetic field was applied perpendicular to ∇T , i.e., out-of-plane to the sample. ANE measurements were taken for the IM configuration by placing the sample upright (Figure 2b). Figure 2c and 2d present the thermopower from the ANE signal (S_{ANE}) and magnetization (\vec{M}) derived from vibrating sample magnetometry (VSM) measurements taken at 350 K in the PM and IM configurations, respectively. The normalized S_{ANE} was defined as follows:

$$S_{ANE} = \frac{E_{ANE}}{\nabla T} = \left(\frac{V_{ANE}}{\Lambda T}\right) / \left(\frac{L}{W}\right),\tag{2}$$

where $V_{\rm ANE}$, L, ΔT , and w are the ANE voltage, the length, the temperature difference, and the width of the samples, respectively. In the IM configuration (Figure 2d), \vec{M} was rapidly saturated with an anisotropy field H of 0.2 T, while this was much slower for the PM configuration (Figure 2c), with a linear increase until saturation and an anisotropy field H of 2 T. These trends for the IM and PM configurations at low temperatures corresponded well with previous reports of ferromagnetic Ni₈₁Fe₁₉/GGG^[24] and FeRh/MgO (001)^[22] substrates. The differences between the two configurations can be explained by the anisotropic magnetoresistance (AMR),^[25, 26] which is clarified further in the Discussion section. We also measured the ANE thermopower by varying ΔT from 0 to 10 K at T = 300 K for the PM and IM configurations while the applied magnetic field was swept from -3 to 3 T (Figure 2e and 2f). In both configurations, the saturation voltage signal derived from V_{ANE} was proportional to ΔT following Equation (2). The amplitude of saturation V_{ANE} before normalization shows different

value between PM and IM configuration. For instance, at $\Delta T = 10$ K, in PM (Figure 2e) $V_{ANE} = 2.2$ V while in IM (Figure 2f) $V_{ANE} = 7.2$ V. This will be briefly discussed in the Supporting Information (Note 1 with Figures S1–S3) with the contribution of ∇T to the ANE thermopower.

To observe the behavior of the ANE thermopower and magnetization during the first-order magnetic phase transition, we took measurements starting at 350 K while lowering the temperature in 25 K intervals to 150 K (Figures 3a–d for the PM configuration and Figures 4a–d for the IM configuration). As shown in Figure 2, the applied temperature gradient and the magnetic field sweep were identical. In the IM configuration (Figure 4a) at 300–350 K, there was significant saturation of the ANE signal $(S_{ANE} = 0.13 \,\mu\text{V/K})$ under a stronger magnetic field, while rapid saturation occurred even at $H < 0.5 \,\text{T}$. Similarly, in the PM configuration (Figure 3a), there was a linear increase in the signal, with saturation $(S_{ANE} = 0.2 \,\mu\text{V/K})$ reached in the higher field region ($H = 2 \,\text{T}$). Equation (1) and (2) show temperature-dependent magnetization, meaning that S_{ANE} and \vec{M} play an important role in determining the ANE thermopower at various temperatures. However, because the system reached the temperature starting from 275 K in both the PM and IM configurations (Figures 3 and 4, respectively), the saturation signal of the ANE thermopower dramatically decreased. This can be explained by the net magnetization \vec{M} decreasing due to the FM–AFM phase transition. Based on this analysis, we identified the transition temperature T_c to be around 250–300 K.

In both Figures 3a–c and Figures 4a–c, unusual S_{ANE} behavior was observed for the mixed magnetic phase in the low-temperature region. The S_{ANE} at 150–250 K is presented in Figures 3b and 4b for both configurations to illustrate this. In this temperature range, the slope of the ANE signal at zero magnetic field was reversed, while at higher fields up to H = 3 T, the slope remained positive, similar to S_{ANE} in the FM state. After the phase transition, the S_{ANE} at 150 K decreases to ~0.03 and ~0.01 μ V/K in the IM and PM configurations, respectively. In addition, because Figures 3a–c and Figures 4a–c

present ANE measurements taken during the cooling process (from 350 to 150 K), we also measured the ANE during the heating cycle (Figures 3d and 4d), showing a clear magnetic phase transition from AFM to FM in the FeRh films. These results correspond well with previous studies involving the sample materials.^[22] For example, epitaxial FeRh thin films deposited on a MgO (001) substrate were reported to have a transition temperature between 200 and 300 K, with the difference in the transition temperature reported in other studies due to the dependence of T_c on the thickness of the film, variation in the mechanical strain effect of different substrates (which is also dependent on the applied magnetic field and temperature). and the Rh content of the thin film. [11, 27-29]

2.3. Magnetic Characterization (M-H) of FeRh Films in IM and PM Configurations

To observe the magnetization characteristics and the relationship between the ANE thermopower and magnetization, we took VSM measurements in the same temperature range from 150–350 K in the IM and PM directions. Figures 5a and b present the magnetization as a function of the applied field for each configuration. To obtain the magnetization of the FeRh thin films, we subtracted the magnetic moment of the Al₂O₃ substrate from the original M-H curve for FeRh/Al₂O₃. The units of the magnetization were estimated by dividing the net magnetic moment from the VSM measurements by the volume of the FeRh film (emu/cm³). The VSM measurements were taken in the temperature range of 150–350 K in 25 K intervals, and the magnetic field was swept from 9 to –9 T and then from –9 to 9 T.

Figure 5c and d present the individual M-H curves for the PM and IM configurations, respectively, according to the temperature. In the PM configuration, there was a gradual increase in magnetization from -3 T to 3 T; in contrast, in the IM configuration (Figure 5d), there was a rapid increase in magnetization in the range of -0.5 T to 0.5 T until it reached saturation. This indicated that the IM configuration had a high magnetic sensitivity due to the easy-axis anisotropy of the FeRh thin film. In

addition, as shown in the M-H curves for the FM state within the range of H = -3 T to 3 T, both configurations exhibited an FM hysteresis loop when the temperature was higher than 300 K. On the other hand, in both configurations, the saturation magnetization was lower for the AFM state ($T \le 250$ K), leading to relatively flat curves, though the slope of the magnetization at H = 0 had a finite value. Both saturation magnetizations in the PM and IM configuration yields almost identical value, $\sim 1.2 \times 10^3$ emu/cm³ at 350 K and $0.1 - 0.2 \times 10^3$ emu/cm³ at 150 K. While most of these features were also observed in the ANE measurements (Figures 3 and 4), one distinct characteristic of the M-H curve (Figure 5) was the magnetization loop in the transition temperature region. For example, in the IM configuration (Figure 5d) within the temperature range of 250–300 K, more than one anisotropy field was present. Saturation was first observed at H = 0.5 T and it then occurred again at H = 9 T. Because clear M-H curves were observed below or above this transition temperature region in the AFM and FM states, amorphous M-H curves with more than one saturation field are an indicator of an intermediate state (i.e., a mixed magnetic phase) that combines FM and AFM. In other words, soft magnet properties (i.e., a slender hysteresis curve such as that shown at T = 350 K on the right side of Figure 5d) in the FM state and relatively hard magnet properties in the AFM state (because a sufficiently strong external magnetic field is required to achieve spin flip-flop in AFM sublattices^[30]) are both present in the temperature region for the magnetic transition. The hysteresis observed at magnetic fields above 0.5 T (Figures 5c and d) provides compelling evidence in support of this explanation, aligning with the findings of previous studies on metamagnetic transitions (i.e., field-induced AFM-to-FM phase transitions). [31, 32]

In general, hard or soft magnet properties other than FM cannot be generally categorized. However, when the temperature is lowered and the system enters a magnetic phase transition, residual FM orders from the Fe atoms in the FeRh thin film exhibit weak soft magnet properties. This is simultaneously perturbed in the AFM matrix by exchange coupling with these residual FM orders.^[33] In addition, AFM magnets may require spin flip—flop fields to reach saturation magnetization. From the M-H curves

measured for the metastate of the FeRh thin films, hard and soft magnetic properties coexist during the first-order magnetic phase transition. This has been phenomenologically reported in other studies by varying the Rh composition ratio (Fe_xRh_{100-x}).^[17, 29] If the content of Rh is significantly higher or lower than Fe, disordered fcc and bcc phases are observed (A1 FeRh and A2 FeRh) rather than the more well-known chemically ordered CsCl structure (B2 FeRh).^[17] Therefore, Rh-rich magnetism yields low magnetization, especially at the interface.^[17]

Variation in the Rh composition ratio can also produce different magnetic phases depending on the layer of the FeRh thin film, especially close to the interface. [17, 29] According to the continuum micromagnetic model reported by Pellicelli *et al.*, strong interface coupling between hard and soft magnet systems can result in more than one saturation point in the magnetic hysteresis loop. [34] Similarly, amorphous M-H curves with more than one coercive field have been suggested in soft FM/weak AF spacer/hard FM exchange-coupled structures. [35] In this work, differences in the composition ratio of Rh in the XPS results measured at different positions within the same sample supported this explanation (Supporting Information Note 6). Finally, unlike the ANE thermopower, neither the PM nor IM magnetization exhibited a reversal in the slope near the zero-field region. Figures 5e and f present the M-T curves for cooling and heating, respectively, with the magnetization measured by lowering and raising the temperature, respectively, under a fixed magnetic field (H = 3 T).

2.4. Magnetic Phase Transition of (110)-oriented FeRh Films in IM and PM Configurations

The ANE and M-H curves for FeRh share common characteristics in both the IM and PM configurations (Figures 2c and d and Figures 3–5). Around zero field (Figures 2c and d) in the IM configuration, both curves tend to switch sign; in particular, when the magnetic field was swept from positive to negative, the saturation signal rapidly dropped near the zero magnetic field point. On the other hand, in the PM

configuration, the ANE and M-H curves both exhibited a gradual fall in saturation when the magnetic field was swept from positive to negative. Because the AMR ($\Delta R/R$) depends on the angle of the rotating magnetization \vec{M} , materials with a relatively high magnetic sensitivity produce a clear AMR because the magnetization is along the easy axis. [25, 26] For example, in-plane angle-dependent AMR measurements of FeRh reported by other studies have revealed continuous AMR signals with a continuous derivative with respect to the angle, indicating that the easy axis is in the IM direction. [36] In the present study, because $V_{ANE} \sim R_{xx}$ (where the subscript xx is the direction in which the ANE is measured and R is the resistance), the more rapid change in the signal observed in Figure 2c compared with Figure 2d suggests that magnetization \vec{M} is more sensitive to a magnetic field applied in the IM direction. Therefore, based on Equation (1), the ANE signal directly follows the magnetization of the system. This trend was also observed at different temperatures (Figures 3 and 4). At temperatures below the Curie temperature (~225 and ~250 K for IM and PM, respectively), this trend starts to become indistinguishable between the two configurations due to the suppressed magnetization in the AFM state of FeRh. There were also clear differences between the ANE signal (Figures 3 and 4) and the M-H curve (Figure 5), where, even under a strong magnetic field, a consistent increase in the ANE signal was observed rather than saturation being reached. This was due to the contribution of the Nernst effect to the ANE. [4] However, this contribution is low, as can be seen from the slope of the ANE curves under a high magnetic field (Figures 4a and b).

Another distinct feature of the ANE signal and M-H curve is that there is a sign reversal in the slope of the curve near zero magnetic field in the ANE signal in the mixed phase. For example, in Figure 2, where the ANE is measured at room temperature, the sign of the slope at zero field is positive. However, in Figures 3a–c (PM configuration) this slope starts to switch its sign below 275 K. This was also observed for the IM configuration (Figures 4a–c), though the sign reversal occurred below 225 K. The

negative slope of the ANE indicates the presence of negative remnant magnetization. Also known as residual magnetization in the AFM state, remnant magnetization usually results from the application of a magnetic field.^[37] Even though, in the ideal colinear AFM state, the net magnetization vanishes yielding zero magnetization \vec{M} , in a real system, the spins in the AFM domains are separated from the colinear AFM state, occasionally exhibiting non-collinearity with respect to the applied field and the anisotropy of the thin film on the substrate. [38, 39] In our case, the intrinsic magnetic anisotropy of the FeRh film can be changed because multiple exchange interactions occur between the residual FM moments and the AFM matrix, resulting in colinear spins in the AFM state that do not perfectly align with the applied field^[40] but rather are re-oriented by minimizing the free energy.^[39] The canted spin phase is an example of this.^[41-43] Previous studies have noted that ferromagnetic layers can form between the substrate and the FeRh film due to the nonuniform chemical ordering arising from Rh-rich or deficient domains or the strain on FeRh depending on the temperature, which contributes to the stabilization of the weak ferromagnetic phase even below the phase transition temperature T_c . [15, 17, 33, 44] However, this cannot explain negative remnant magnetization at temperatures below T_c in FeRh films (Figure S6 in Supporting Information Note 4). Therefore, another mechanism is necessary to explain this abnormal behavior in FeRh films.

We also analyzed the M-H curves of the FeRh films in both the IM and PM configurations (Figure 5). As shown in Figure 5, we did not observe any sign reversal in the magnetization at temperatures below T_c . Consequently, based on the difference between the ANE signal and the M-H curve for FeRh, the effect of the substrate should be considered. We thus analyzed the M-H curves of the Al_2O_3 substrate (Figure S5 in Supporting Information Note 1) and took ANE thermopower measurements of FeRh on a SiO_2/Si substrate (Figure S4 in Supporting Information Note 1). No sign reversal for the ANE signal due to the negative remnant magnetization at low temperatures down to 85 K was observed for the FeRh/SiO₂/Si structure. Because SiO_2/Si is a weakly diamagnetic material while Al_2O_3 exhibits

diamagnetic properties, these results indicate that the substrate plays a significant role in the ANE signals of FeRh films. While the substrate has been suggested to contribute to the surface anisotropy or intrinsic strain effect due to the lattice mismatch with epitaxially grown FeRh films (which results in a magneto-structural effect as the material is heated or cooled),^[11, 45] we suggest that the substrate has an effect in terms of the long-range interaction between the diamagnetic spins in Al₂O₃ and those of the FeRh film.

3. Discussion

To further investigate the role of the substrate in the magnetic phase transition of the FeRh films, we investigated the abnormally ordered phase of spins under different temperature regimes using FEM simulations. Because the simulation of the temperature hysteresis of FeRh magnetization requires adiabatic heat exchange between the sample, holder module, and chamber in the PPMS for each temperature, we used a laser-heating method that has been employed in time-resolved analysis for more rapid simulations. [46] In general, the use of a pump–probe technique with a single pump leads to lattice expansion due to laser-induced heating. [47,48] The phenomenological similarity between the ultrafast spin dynamics of laser-induced heating and LLG dynamics is briefly explained in Supporting Information Notes 2 and 3. From an FEM modeling perspective, magnetization \vec{M} is the basic quantity of interest. Thus, COMSOL 6.0 Multiphysics was employed using an add-on micromagnetic module based on LLG dynamics. [49-52] A 2 × 2 unit cell of spins representing the spins at Fe sites was set with the exchange energy parameter J taken from previous studies. For example, in the AFM state, J is negative and proportional to $\sim m_A m_B$ (where A and B denote the sublattices in the 2 × 2 unit cell). [30] The spins at the Rh site were not considered in this study. Instead, these were replaced by Fe-Fe pairs gaining additional exchange energy J when the system undergoes a first-order phase transition (Supporting

Information Note 4). This is reasonable because Equation (4) usually underestimates the effect of the magnetic field on the induced magnetic moment in Rh atoms.^[53] We set J_{Fe-Fe} at -5 meV and J_{Fe-Rh} (which is the change in J_{Fe-Fe} when the system undergoes a first-order phase transition) at 13 meV.^[53]

Figure 6 displays the overall numerical simulation results for the spin configurations in terms of magnetization \vec{m} . In particular, Figures 6a and d present the change in unit magnetization \vec{m} as the laser-induced heating time increases in the IM and PM configurations, respectively, while Figures 6b and e present the spins for the AFM and FM states in the IM and PM configurations, respectively. Figure 6c presents the 2D color distribution of the spin orientations at each time step, with each corresponding to the point of time indicated in Roman letters in Figure 6a. Over time, the growth in magnetization led to the nucleation of the spin-down regions, while the spin-up regions expanded into the entire 2×2 cell. Note that, in Figures 6a–c (IM) and Figures 6d–f (PM) a field of 3 T is applied in the spin-up direction (i.e., the direction in which the spins in the FM state point). This is the reason that the spin-down states at time step I were not a pure blue color. On the other hand, though Figures 5c and d show that easy-axis magnetization occurs in the IM configuration, both Figures 6a and c exhibit similar shapes in the growth of magnetization during the heating process. These features were also observed for the temperature-dependent magnetization curves in the IM and PM configurations (Figures 5e and f). This may indicate that, in both configurations, there was a primary response in the change of the exchange interaction J originating from lattice expansion during the heating process.

We also conducted other simulations that included long-range interactions between the spins in the original 2×2 cell and diamagnetic spins at the bottom of the cell (Supporting Information Note 5). Given spins \vec{s} from the magnetization in the different region, noted as the distance (= x - y) with the coordinates x and y, the long-range interaction is given as^[37]

$$\int dx \, dy \, \frac{\vec{s}(x) \cdot \vec{s}(y)}{|x - y|^{d + \sigma}} \,, \tag{3}$$

where d denotes the dimensions, and σ is the constant from the Fisher relation.^[54] Equation (3) indicates that the exchange interaction energy J decays algebraically over distance, i.e. $J_{\langle ij \rangle} \sim \left(\frac{1}{r_{ii}}\right)^{d+\sigma} J_a$ with a cutoff distance $r = r_c$. [55] Here, $\vec{s}(x)$ denotes the spins in the Fe lattice, while $\vec{s}(y)$ denotes the spins in the diamagnetic Al₂O₃ substrate layer. The magnitude of the diamagnetic spins was set according to the M-H curves derived from Al₂O₃, with the magnitude of the initial magnetization vector relatively low compared to the spins for Fe. By including Equation (3) to the form of the exchange energy, Figure 6g was obtained from the simulation results at $\sigma = 0.3$. Unlike the previous calculations, no external magnetic field was applied to observe the relationship between the sign reversal around the zero-field region in the ANE measurements and the long-range interactions. It was observed that, before the magnetic phase transition, a net negative residual region in the magnetization was present (Figure 6g), which corresponded to the negative slope around zero field demonstrated by the ANE signal in the experiment. From the equation $\vec{E}_{ANE} = Q_{ANE} \vec{M} \times \nabla T$, we extracted Q_{ANE} using the saturation magnetization and temperature gradient from the experiment. Q_{ANE} also exhibited a negative value at low temperatures due to negative remnant magnetization (Figure 6k). Additionally, Figure 6i shows more complicated color contours for the spin orientations compared with Figures 6c and f. This is obviously identified in the AFM state, where multiple spin orientations are indicated by the mixture of contour colors in a single cell. For this reason, we sub-divided the number of spins in each individual cell while not affecting the overall to average out the magnetization in the cell.

Furthermore, we performed the same simulations under an applied magnetic field of H = 3 T while considering the long-range interactions with the substrate. No negative remnant magnetization was observed (Figures 6l and n). The sign reversal only occurred around zero magnetic field. Finally, we conducted a magnetic field-sweep simulation while keeping the temperature fixed at the AFM state

(Figure 6j). A sign reversal was clearly observed around zero field with the disordered spins in the AFM state (Figure 6m). Magnus *et al.* introduced long-range interactions as a means to qualitatively explain the long-range ferromagnetic order established in exchange spring-magnet structures where the two ferromagnetic layers are separated by a non-magnetic layer. This calculation with aid of the spin Heisenberg model was also adopted in other studies to obtain critical exponents for magnetization depending on the temperature. This suggested the possibility of the weak magnetic order of diamagnetic Al_2O_3 playing a role in the direct exchange coupling with the adjacent AFM order. However, the long-range interaction is based on the proximity effect, which has a mutual influence between the adjacent magnetic orderings. In addition, studies on exchange spring magnets set the exchange interaction energy J at a low value for the non-magnetic layer. It is thus reasonable to consider the long-range interaction between the magnetic order of the substrate and that of the original film and conclude that this interaction results in a more complex magnetic texture that contributes to the unusual remnant magnetization.

4. Conclusion

In summary, we measured the ANE thermopower of (110)-oriented FeRh films grown on an Al₂O₃ substrate. ANE measurements are a suitable method for capturing thermally driven magnetic phase transitions. Materials exhibiting magnetic phase transitions also provide insight into ANE measurements, demonstrating the temperature dependence of the thermopower due to the differences in the magnetic textures between the FM and AFM states. Furthermore, the substrate effect plays an important role in the abnormal behavior of the ANE signal in the mixed phase at low temperatures in both the PM and IM configurations. The key reason proposed for the negative remnant magnetization in the AFM state is the long-range interaction between the original spins in FeRh and those in the diamagnetic Al₂O₃ substrate.

Future research should theoretically investigate the association of this long-range interaction with the originally reported emerging anisotropy attributed to mechanical and structural changes during the phase transition, such as the high-order terms in the magnetic anisotropy within a particular temperature range leading to the re-orientation of the spin textures or the magnetic order of the magnetic thin films.^[39]

5. Experimental Section

Material growth and characterization: In this study, (110)-oriented FeRh films were grown to a thickness of 25–30 nm on Al₂O₃ and SiO₂/Si substrates using a DC magnetron sputtering system, with their successful growth confirmed using the X-ray reflectivity, HR-TEM, and STEM analyses. Prior to the growth of the FeRh layer, the substrate was cleaned to remove organic contaminants on the surface in an Ar atmosphere with a pressure of 1 × 10⁻² Torr and an RF power of 10 W. The FeRh films were produced with a DC power of 75 W and a working Ar pressure of 4 × 10⁻³ Torr using a stoichiometric FeRh sintered 2-inch target. Following film growth at 630 °C with a sputtering rate of ~0.04 nm/s, the film underwent annealing at an elevated temperature of 730 °C for 1 h in a high-vacuum environment with a pressure of approximately 4 × 10⁻⁸ Torr. The crystalline quality of the FeRh was evaluated using XRD (Figures 1a and b), cross-sectional HR-TEM (Figures 1c–f) and scanning-TEM (STEM, Figures 1g-k). Cross-sectional STEM analysis was also conducted with energy-dispersive X-ray mapping (Figures 1l–n) and XPS (Figure 1o) to assess the interface and to determine the composition and atomic ratio of the Fe and Rh in the films, respectively. Further details on the material growth process are available in our previous reports.^[8, 58]

ANE and M-H measurements: We used aluminum nitride (AlN) plates in the ANE measurement setup because of its high thermal conductivity and electrical insulation properties (Figure 2a). A resistor (100 Ω) was affixed to the top of the holder to generate a consistent temperature differential across the sample. The desired ∇T was controlled using thermocouple junctions bonded to both the upper and lower sections of the holder, ensuring a steady state during the measurements (Figure 2a). It was confirmed that the effects of the magnetic field and temperature on the holder were negligible (Supporting Information Note 1). As shown in Figure 2a, the upper ANE measurement module was mounted on a PPMS (DynaCool, Quantum Design, Inc. USA) copper puck. In addition, the magnetization characteristics of the sample were recorded in both IM and PM directions (Figure 2b), and we took VSM measurements using the VSM option in the PPMS in the same temperature range from 100 to 350 K. All of the ANE data were controlled and performed using CompackDAQ with LabView software (National Instruments, Inc. USA).

Numerical calculations with FEM (COMSOL): The q-states Potts model for J>0 (the FM state) and J<0 (the AFM state) can be written as

$$H = -J \sum_{\langle i,j \rangle} \delta_{\sigma_i \sigma_j} - \vec{h} \cdot \sum_i \delta_{\sigma_i,1}, \tag{4}$$

where $\delta_{\sigma_l \sigma_j} = \frac{1}{q} (1 + (q - 1) e^{\sigma_l} \cdot e^{\sigma_j})$ and the additional term in \vec{h} represents the contribution of the applied magnetic field. [59] The sign of the exchange energy J depends on the FM or AFM state. The FM state q=2 Potts model is simply the Ising model for FM, and this was also the case for AFM. In the case of the q=3 Potts model, it can be substituted with the Ising model with $\vec{s_l} = \binom{1}{0}, \binom{-1/2}{\sqrt{3/2}}, \binom{-1/2}{\sqrt{3/2}}$ [60] In our model simulation, we partially utilized the q=2 Potts model for the pure FM and AFM states. [53, 61] The intermediate states between the pure AFM and FM states were represented by changing the value of J over time. A microscopic connection between the LLG model and the exchange spin model can be achieved when the free energy F obtained from the Heisenberg spin models leads to the effective field \vec{H}_{eff} , and the term yields the overall time-traced dynamics of the magnetization in the form of LLG equation. The model Hamiltonian for all sublattices in our 2×2 cell can be expressed as follows: [62]

$$\beta H = -J \sum_{\langle i \in A, j \in B \rangle} \vec{s}_i^A \cdot \vec{s}_i^B - J \sum_{\langle i \in B, j \in A \rangle} \vec{s}_i^B \cdot \vec{s}_i^A, \tag{5}$$

where $\beta = 1/k_BT$, in which k_B is the Boltzmann constant. A pure FM or AFM state is determined by the sign of J. In calculating the mean-field approach for the free energy (F), saddle point approximation was employed. Our 2 × 2 cell contained two sublattices, A and B. Thus, the mean-field Hamiltonian can be expressed as

$$\beta H = -\sum_{i \in A} \overrightarrow{h_A} \cdot \overrightarrow{s_i}^A - \sum_{i \in B} \overrightarrow{h_B} \cdot \overrightarrow{s_i}^B , \qquad (6)$$

where h_A and h_B are the microscopic effective fields acting on the spins of sublattices A and B, respectively. Consequently, the free energy is calculated from Equation (6) using the partition function for A and B. Based on saddle point approximation or Gibbs inequality, $\beta F \leq \beta F_0 + \langle \beta H - \beta H_0 \rangle_0$ and, by differentiating the explicit free energy by \vec{m} , effective field \vec{H}_{eff} can be phenomenologically calculated.^[37,62]

$$\vec{H}_{eff\,A(B)} = -\frac{1}{\beta} L^{-1} \{ \vec{m}_{A\,(B)} \} + J_{eff} \, \vec{m}_{B(A)} + \, \vec{H}_{ext} \,, \tag{7}$$

while $\overline{m}_{A(B)}$ is derived from the statistical average of \overline{s} . Here, L(x) is a Langevin function, with L(x) = coth(x) - 1/x. The effective fields for A and B are used in the FEM simulations as input for the LLG equation. In addition, the magnetic anisotropy, which is one of the inputs for the micromagnetic module, is estimated using the M-H curve in Figure 5, where the anisotropy field (H_k) is the minimum field required to reach the saturation magnetization (M_s) . Based on this relation, the anisotropy energy K can be estimated. The timescale of the pump-probe delay during laser heating depends on the laser fluence (J/m^2) . Because our COMSOL micromagnetic module does not have any material-dependent physical properties, we arbitrarily selected time steps of ~50 ps to avoid excessive Newton iterations. We also normalized the units, e.g., the unit magnetic moment, to correspond to the initial magnetization vector, which was normalized to 1. The Gilbert damping parameter α used in the simulations was set to be higher than the typical value for most magnetic materials to ensure rapid relaxation and more rapid

simulations.^[64] The total magnetization \vec{m} for each heating/cooling time step was obtained by averaging out the magnitude of the spins in two of the 2 × 2 cell volumes. The reason for averaging out the magnetization in at least two cells was that, in the AFM state, the antiparallel spins in the two sublattices usually yielded low or vanishing net magnetization \vec{m} when summed.

Supporting Information

Supporting Information is available from the Wiley Online Library or from the author.

Acknowledgements

This study was supported by the National Research Foundation of Korea, funded by the Korean government (2020R1A5A1016518 and 2023R1A2C22002630). This work was also supported by Office of Naval Research 6.1 Base Funding at the U.S. Naval Research Laboratory. M.S.A., and M. Z. acknowledge the support by NSF, grant number 2230352. S.L. and J.C. also thank Prof. E. Saitoh and Dr. Kikkawa for their advices on the ANE measurements. S.L. also thanks Dr. W.L. for his advice for the analysis and figures.

Author contributions

S.L. conceived and designed the entire research project. J.C. and C.P. took the ANE thermopower and VSM measurements with the analysis. G.K. conducted material characterization including TEM, STEM, EDS, and XPS measurements and analysis. J.C., N.P., Y.K., and M.A. performed electrical

characterization. M.J. and S.C. performed XRD characterization for the samples. B.S. and S.B. prepared the FeRh films on both Al₂O₃ and SiO₂/Si substrates via sputtering and performed optical characterization. J.P., C.P., and J.C. prepared the samples for the PPMS measurements. S.C., B.S., S.B., M.Z., G.K., and S.L. supervised the experiments, including the sample growth, optical measurements, material characterization, and ANE thermopower and thermoelectric measurements. J.C., C.P., G.S., and S.L. participated in the analysis of the ANE characterization in spin thermal transport. J.C., C.P., G.S., and S.L. co-wrote the manuscript. All of the authors discussed the results and commented on the manuscript.

Conflict of Interest

The authors declare no conflict of interest.

Keywords

Ferromagnetic materials, magnetic phase transition, (110)-oriented FeRh films, anomalous Nernst effect, temperature-dependent magnetization-magnetic field strength (M-H), finite element method, Heisenberg spin model, Landau-Lifshitz-Gilbert equation

References

- 1. Boona, S. R.; Jin, H.; Watzman, S., J. Appl. Phys. 2021, 130, 171101.
- 2. Mizuguchi, M.; Nakatsuji, S., Sci. Technol. Adv. Mater. 2019, 20, 262.
- 3. Ohnuma, Y.; Matsuo, M.; Maekawa, S., *Phys. Rev. B* **2017**, *96*, 134412.
- 4. Ramos, R.; Aguirre, M. H.; Anadón, A.; Blasco, J.; Lucas, I.; Uchida, K.; Algarabel, P. A.; Morellón, L.; Saitoh, E.; Ibarra, M. R., *Phys. Rev. B* **2014**, *90*, 054422.
- 5. Wang, Y.; Decker, M. M.; Meier, T. N. G.; Chen, X.; Song, C.; Grunbaum, T.; Zhao, W. W.; Zhang, J.; Chen, L. B.; Back, C. H., *Nat. Commun.* **2020**, *11*, 275.
- 6. Mariager, S. O.; Pressacco, F.; Ingold, G.; Caviezel, A.; Mohr-Vorobeva, E.; Beaud, P.; Johnson, S. L.; Milne, C., H.; Mancini, E.; Moyerman, S.; Fullerton, E. E.; Feidenhans'l, R.; Back, C. H.; Quitmann, C., *Phys. Rev. Lett.* **2012**, *108*, 087201.
- 7. Chen, X. Z.; Feng, J. F.; Wang, Z. C.; Zhang, J.; Zhong, X. Y.; SOng, C.; L., J.; Zhang, B.; F., L.; Jiang, M.; Tan, Y. Z.; Zhou, X. J.; Shi, G. Y.; Zhou, X. F.; Han, X. D.; Mao, S. C.; Chen, Y. H.; Han, X. F.; Pan, F., *Nat. Commun.* **2017**, *8*, 449.
- 8. Cress, C. D.; Wickramaratne, D.; Rosenberger, M. R.; Hennighausen, Z.; Callahan, P. G.; LaGasse, S. W.; Bernstein, N.; Erve, O. M.; Johker, B. T.; Qadri, S. B.; Prestigiacomo, J. C.; Currier, M.; Mazin, I. I.; S.P., B., ACS Appl. Mater. Interfaces 2021, 13, 836.
- 9. Feng, Y.; Fukuda, T.; Kakeshita, T., *Intermetallics* **2013**, *36*, 57.
- 10. Bordel, C.; Juraszek, J.; Cooke, D. W.; Baldasseroni, C.; Mankovsky, S.; Minar, J.; Ebert, H.; Moyerman, S.; Fullerton, E. E.; Hellman, F., *Phys. Rev. Lett.* **2012**, *109*, 117201.
- 11. Ceballos, A.; Chen, Z.; Schneider, O.; Bordel, C.; Wang, L.-W.; Hellman, F., *Appl. Phys. Lett.* **2017**, *111*, 172401.
- 12. Seifert, T.; Martens, U.; Günther, S.; Schoen, M. A. W.; Radu, F.; Chen, X. Z.; Lucas, I.; Ramos, R.; Aguirre, M. H.; Algarabel, P. A.; Anadón, A.; Körner, H. S.; Walowski, J.; Back, C.; Ibarra, M. R.; Morellón, L.; Saitoh, E.; Wolf, M.; Song, C.; Uchida, K.; Münzenberg, M.; Radu, I.; Kampfrath, T., SPIN 2017, 7, 1740010.
- 13. Han, L.; Wang, Y.; Zhu, W.; Zhao, R.; Chen, X.; Su, R.; Zhou, Y.; Bai, H.; Wang, Q.; You, Y., *Sci. Adv.* **2022**, *8*, eabq2742.
- 14. Popescu, A.; Rodriguez-Lopez, P.; Haney, P. M.; Woods, L. M., *Phys Rev B* **2018**, *97*, 140407(R).
- 15. Saglam, H.; Liu, C.; Li, Y.; Sklenar, J.; Gibbons, J.; Hong, D.; Karakas, V.; Pearson, J. E.; Ozatay, O.; Zhang, W., arXiv preprint arXiv:2012.14383 2020,
- 16. Zhang, S.; Xia, S.; Li, Q.; Yang, B.; Li, J.; Cao, Q.; Wang, D.; Liu, R.; Du, Y., *Appl. Phys. Lett.* **2021**, *118*, 142401.
- 17. Ye, J.; Hauke, M.; Singh, V.; Rawat, R.; Gupta, M.; Tayal, A.; Amir, S. M.; Stahn, J.; Paul, A., *RSC Adv.* **2017**, *7*, 44097.
- 18. Kumar, H.; Cornejo, D. R.; Morelhao, S. L.; Kycia, S.; Montellano, I.; Alvarez, N. R.; Alejandro, G.; Butera, A., *J. Appl. Phys.* **2018**, *124*, 085306.
- 19. Kumar, H.; Morelhao, S. L.; Pessotto, G.; Singh, H.; Sinha, A. K.; Cornejo, D. R., *J. Magn. Magn. Mater.* **2022**, *556*, 169442.
- 20. Mei, A. B.; Gray, I.; Tang, Y.; Schubert, J.; Werder, D.; Bartell, J.; Ralph, D. C.; Fuchs, G. D.; Schlom, D. G., *Adv. Mater.* **2020**, *32*, 2001080.
- 21. Wu, H.; Zhang, H.; Wang, B.; Groß, F.; Yang, C.-Y.; Li, G.; Guo, C.; He, H.; Wong, K.; Wu, D., *Nat. Commun.* **2022**, *13*, 1629.
- 22. Cao, C. M.; Chen, S. W.; Cui, B. S.; Yu, G. Q.; Jiang, C. H.; Yang, Z. Z.; Qiu, X. P.; Shang, T.; Xu, Y.; Zhan, Q. F., *ACS nano* **2022**, *16*, 12727.
- 23. Song, S.; Cho, C.-w.; Kim, J.; Lee, J.; Lee, D.; Kim, D.; Kim, H.; Kang, H.; Park, C.-H.; Park, J.

- K., J. Alloy. Compd. 2022, 901, 163611.
- 24. Kikkawa, T.; Uchida, K.; Daimon, S.; Shiomi, Y.; Adachi, H.; Qiu, Z.; Hou, D.; Jin, X. F.; Maekawa, S.; Saitoh, E., *Phys. Rev. B* **2013**, *88*, 214403.
- 25. Inoue, J.-i., Nanomagnetism and Spintronics: 2. GMR, TMR, BMR, and Related Phenomena. Elsevier Inc. Chapters: 2013.
- 26. Ritzinger, P.; Vyborny, K., R. Soc. Open Sci. 2023, 10, 230564.
- 27. Maat, S.; Thiele, J.-U.; Fullerton, E. E., *Phys. Rev. B* **2005**, *72*, 214432.
- 28. Xie, Y.; Zhan, Q.; Shang, T.; Yang, H.; Wang, B.; Tang, J.; Li, R.-W., AIP Adv. 2017, 7, 056314.
- 29. Yamauchi, T.; Hamada, Y.; Kurokawa, Y.; Yuasa, H., Jpn. J. Appl. Phys. 2022, 61, Sc1019.
- 30. Baltz, V.; Manchon, A.; Tsoi, M.; Moriyama, T.; Ono, T.; Tserkovnyak, Y., *Rev. Mod. Phys.* **2018**, *90*, 015005.
- 31. Elovaara, T.; Huhtinen, H.; Majumdar, S.; Paturi, P., J. Phys.-Condes. Matter 2012, 24, 216002.
- 32. Ziese, M.; Vrejoiu, I.; Hesse, D., Appl. Phys. Lett. 2010, 97, 052504.
- 33. Fan, R.; Kinane, C. J.; Charlton, T. R.; Dorner, R.; Ali, M.; de Vries, M. A.; Brydson, R. M. D.; Marrows, C. H.; Hickey, B. J.; Arena, D. A.; Tanner, B. K.; Nisbet, G.; Langridge, S., *Phys. Rev. B* **2010**, *82*, 184418.
- 34. Pellicelli, R.; Solzi, M.; Pernechele, C.; Ghidini, M., *Phys. Rev. B* **2011**, *83*, 054434.
- 35. Polishchuk, D.; Tykhonenko-Polishchuk, Y. O.; Lytvynenko, Y. M.; Rostas, A.; Kuncser, V.; Kravets, A.; Tovstolytkin, A.; Gomonay, O.; Korenivski, V., *arXiv preprint arXiv:2303.09301* **2023**,
- 36. Sklenar, J.; Shim, S.; Saglam, H.; Oh, J.; Vergniory, M. G.; Hoffmann, A.; Bradlyn, B.; Mason, N.; Gilbert, M. J., *Commun. Phys.* **2023**, *6*, 241.
- 37. Kardar, M., Statistical physics of fields. Cambridge University Press: 2007.
- 38. Chen, X.; Shi, S.; Shi, G.; Fan, X.; Song, C.; Zhou, X.; Bai, H.; Liao, L.; Zhou, Y.; Zhang, H.; Li, A.; Chen, Y.; Han, X.; Jiang, S.; Zhu, Z.; Wu, H.; Wang, X.; Xue, D.; Yang, H.; Pan, F., *Nat. Mater.* **2021**, *20*, 800.
- 39. Usadel, K. D.; Hucht, A., Phys. Rev. B 2002, 66, 024419.
- 40. Zhu, X.; Li, Y.; Xie, Y.; Qiu, Q.; Cao, C.; Hu, X.; Xie, W.; Shang, T.; Xu, Y.; Sun, L.; Cheng, W.; Jiang, D.; Zhan, Q., *J. Alloy. Compd.* **2022**, *917*, 165566.
- 41. Kudrnovsky, J.; Drchal, V.; Turek, I., Phys. Rev. B 2015, 91, 014435.
- 42. Kovalev, A. S.; Prilepsky, J. E.; Kryukov, E. A.; Kulik, N. V., Low Temp. Phys. **2010**, *36*, 831.
- 43. Buzdakov, A. G.; Dolgikh, I. A.; Zvezdin, K. A.; Zvezdin, A. K.; Rubi, K.; Zeitler, U.; Christianen, P. C. M.; Rasing, T.; Patel, S. K. K.; Medapalli, R.; Fullerton, E. E.; Dilmieva, E. T.; Kimel, A. V., *Phys. Rev. B* **2023**, *108*, 184420.
- 44. Odkhuu, D., IEEE Trans. Magn. 2019, 55, 1.
- 45. Kim, J. W.; Ryan, P. J.; Ding, Y.; Lewis, L. H.; Ali, M.; Kinane, C. J.; Hickey, B. J.; Marrows, C. H.; Arena, D. A., *Appl. Phys. Lett.* **2009**, *95*, 222515.
- 46. Radu, I.; Stamm, C.; Pontius, N.; Kachel, T.; Ramm, P.; Thiele, J. U.; Dürr, H. A.; Back, C. H., *Phys. Rev. B* **2010**, *81*, 104415.
- 47. Eesley, G. L., *Phys. Rev. B* **1986**, *33*, 2144.
- 48. Ahn, Y.; Zhang, J.; Chu, Z.; Walko, D. A.; Hruszkewycz, S. O.; Fullerton, E. E.; Evans, P. G.; Wen, H., *ACS nano* **2023**, *17*, 18843.
- 49. Lan, J.; Yu, W.; Wu, R.; Xiao, J., Phys. Rev. X 2015, 5, 041049.
- 50. Lan, J.; Yu, W.; Xiao, J., Nat. Commun. 2017, 8, 178.
- 51. Yu, W.; Lan, J.; Xiao, J., Phys. Rev. B 2018, 98, 144422.
- 52. Daniels, M. W.; Yu, W.; Cheng, R.; Xiao, J.; Xiao, D., *Phys. Rev. B* **2019**, *99*, 224433.
- 53. Tran, H. B.; Fukushima, T.; Momida, H.; Sato, K.; Makino, Y.; Oguchi, T., *J. Alloy. Compd.* **2022**, 926, 166718.

- 54. Fisher, M. E.; Ma, S.-k.; Nickel, B., Phys. Rev. Lett. 1972, 29, 917.
- 55. Magnus, F.; Brooks-Bartlett, M. E.; Moubah, R.; Procter, R. A.; Andersson, G.; Hase, T. P.; Banks, S. T.; Hjorvarsson, B., *Nat. Commun.* **2016**, *7*, 11931.
- 56. Ribeiro, M.; Gentile, G.; Marty, A.; Dosenovic, D.; Okuno, H.; Vergnaud, C.; Jacquot, J.-F.; Jalabert, D.; Longo, D.; Ohresser, P.; Hallal, A.; Chshiev, M.; Boulle, O.; Bonell, F.; Jamet, M., *npj* 2D Mater. Appl. **2022**, *6*, 10.
- 57. Wang, R.; Mills, D., Phys. Rev. B 1992, 46, 11681.
- 58. Cress, C. D.; Erve, O.; Prestigiacomo, J.; LaGasse, S. W.; Glavic, A.; Lauter, V.; Bennett, S. P., *J. Mater. Chem. C* **2023**, *11*, 903.
- 59. Wu, F.-Y., Rev. Mod. Phys. 1982, 54, 235.
- 60. Yeomans, J. M., Statistical mechanics of phase transitions. Clarendon Press: 1992.
- 61. Tran, H. B.; Fukushima, T.; Sato, K.; Makino, Y.; Oguchi, T., J. Alloy. Compd. 2021, 854, 157063.
- 62. Mentink, J. H.; Hellsvik, J.; Afanasiev, D.; Ivanov, B.; Kirilyuk, A.; Kimel, A.; Eriksson, O.; Katsnelson, M.; Rasing, T., *Phys. Rev. Lett.* **2012**, *108*, 057202.
- 63. Mathews, S. A.; Prestigiacomo, J., J. Magn. Magn. Mater. 2023, 566, 170314.
- 64. Uchida, K.-i.; Ohe, J.-i.; Kikkawa, T.; Daimon, S.; Hou, D.; Qiu, Z.; Saitoh, E., *Phys. Rev. B* **2015**, 92, 014415.

Figure captions

Figure 1 | Material characteristics of the FeRh thin film on a c-plane Al₂O₃(0001) substrate.

(a) HR-XRD patterns for the FeRh thin film grown on c-plane Al₂O₃ (0001). (b) 2θ-fixed ω-rocking curve scan of the (110) XRD peak. (c) Cross-sectional HRTEM images of the FeRh thin film. (d–f) Enlarged HR-TEM image and corresponding fast Fourier transform (FFT) patterns of the A (yellow-dotted square) and B (red-dotted square) regions in (d), respectively. (g–i) Atomic-resolution annual dark-field scanning TEM (ADF-STEM) images of FeRh/Al₂O₃, FeRh (C, yellow-dotted square), and Al₂O₃ (D, red-dotted square) regions along the [1120] zone axis of Al₂O₃, respectively. (j, k) ADF-STEM images of FeRh along the [011] zone axis of FeRh. (l-n) ABF-STEM image of the 25-nm-thick FeRh thin film and corresponding elemental mappings of Fe (K-line, purple) and Rh (L-line, green),

respectively. (o) Deconvoluted XPS spectra of the Fe 2p and Rh 3d core levels using Gaussian-

Lorentzian curve fitting after Shirley background correction.

Figure 2 | ANE measurement of FeRh films in the PM and IM configurations. (a) and (b) Schematic images of the ANE measurement set-up and both PM and IM configurations mounted between AIN plates for ANE measurements, respectively. A heater (100 Ω resistor) produces the temperature gradient (∇T) for the ANE measurements, while two E-type thermocouples measure the temperature difference across the sample. (c) and (d) Normalized ANE thermopower (black line) and magnetization (red line) as a function of the applied magnetic field (-3 T to +3 T and from +3 T to -3 T) for the FeRh/Al₂O₃ samples at 350 K in the PM and IM configurations, respectively. (e) and (f) ANE voltage signals as a function of the magnetic field (\pm 3 T) and temperature difference of Δ T = 0–10 K (steps of 2 K) for (110)-oriented FeRh films on Al₂O₃ at 300 K in both the PM and IM configurations, respectively.

Figure 3 | Temperature-dependent ANE measurements of FeRh films in a PM configuration. (a) ANE thermopower of FeRh films on an Al₂O₃ substrate as a function of the applied magnetic field up to 3 T in the temperature range of 150–350 K. The arrows denote the sweep direction of the magnetic field (positive or negative). (b) shows all ANE thermopowers of the samples in one figure in PM configuration shown in (a). (c) ANE thermopower of the samples in the low temperature range of 150–250 K, clearly showing the negative slope at the low field H (\sim 0.2 T). (d) ANE voltages (V_{ANE}) in PM configuration with varying temperature during heating (red curve) / cooling cycle (blue curve).

Figure 4 | Temperature-dependent ANE measurement of FeRh films in an IM configuration. (a) ANE thermopower of FeRh films on an Al₂O₃ substrate as a function of the applied magnetic field up to 3 T in the temperature range of 150–350 K. The arrows denote the sweep direction of the magnetic field (positive or negative). (b) ANE thermopower of the samples in the IM configuration shown in (a). (c) ANE thermopower of the samples in the low temperature range of 150–250 K, clearly showing a negative slope at $H = \sim 0.2$ T. (d) ANE voltages (V_{ANE}) in the IM configuration during heating (red) and cooling (blue) cycles.

Figure 5 | Magnetization characteristics of FeRh films. (a)–(c) and (b)–(d) Temperature-dependent magnetization of FeRh films in a magnetic field up to \pm 9 T in both the PM and IM configurations, respectively. The measurements were taken using a PPMS system with a vibrating sample magnetometer (VSM) (Quantum Design, Inc. USA) in the temperature range of 150–350 K. The images on the right of (c) and (d) show an enlargement of the M-H curve for the shaded area (red; H= - 3T to 3T) on the left of (c) and (d), respectively, for different temperatures. (e) and (f) M-T curves for

(110)-oriented FeRh films at a fixed magnetic field of 3 T in both the PM and IM configurations, respectively. The temperature was first swept from 350 to 150 K (cooling) and then from 150 to 350 K (heating) in both configurations. The insets in (e) and (f) show schematic images of both the PM and IM configurations in the VSM measurements. Note that the magnetization of the FeRh film is obtained by subtracting the Al₂O₃ contribution from the originally measured FeRh/Al₂O₃ magnetization.

Figure 6 | FEM calculation results for first-order phase transition in LLG dynamics. (a) Average unit magnetization \vec{m}_{χ} under laser-induced heating in the IM configuration. (b) Spins aligned parallel (antiparallel) to each other in the FM (AFM) phase in the IM configuration. (c) Color distributions of the unit spin orientation at each time step. In the AFM state, spin-up (red) and spin-down (blue) alternate while, in the FM state, the spin-up (red) nucleates the spin-down (blue) domains. (d)–(f). The calculations performed in (a)–(c) are repeated for the PM configuration. (g) Calculation results for \vec{m}_x when including long-range interaction from the substrate. Negative magnetization is observed immediately before and after the magnetic phase transition during heating and cooling, respectively. (h) Spin textures obtained from the AFM/FM states in (g). Spins in the AFM align in a non-colinear manner due to the interaction with the diamagnetic spins from the substrate. (i) Color distribution of the spin orientation obtained from (g). More complicated contours are observed due to the spins from the Al₂O₃ substrate. (j) Magnetic field sweep for a fixed temperature. By including long-range interaction, the sign reversal of the magnetization around zero magnetic field is simulated. (k) Extracted Nernst coefficients Q_{ANE} from ANE measurements. The sign is negative at low temperatures. (1) Simulated average unit magnetization $\overrightarrow{m}_{\chi}$ under long-range interaction when a finite magnetic field of H=3T is applied. When compared with (g), no negative magnetization is observed. (m) Disordered spin textures in the AFM state under a low magnetic field from (j) at time steps I–V. (n) Spin textures in (j) at time steps I–III.

Figure 1

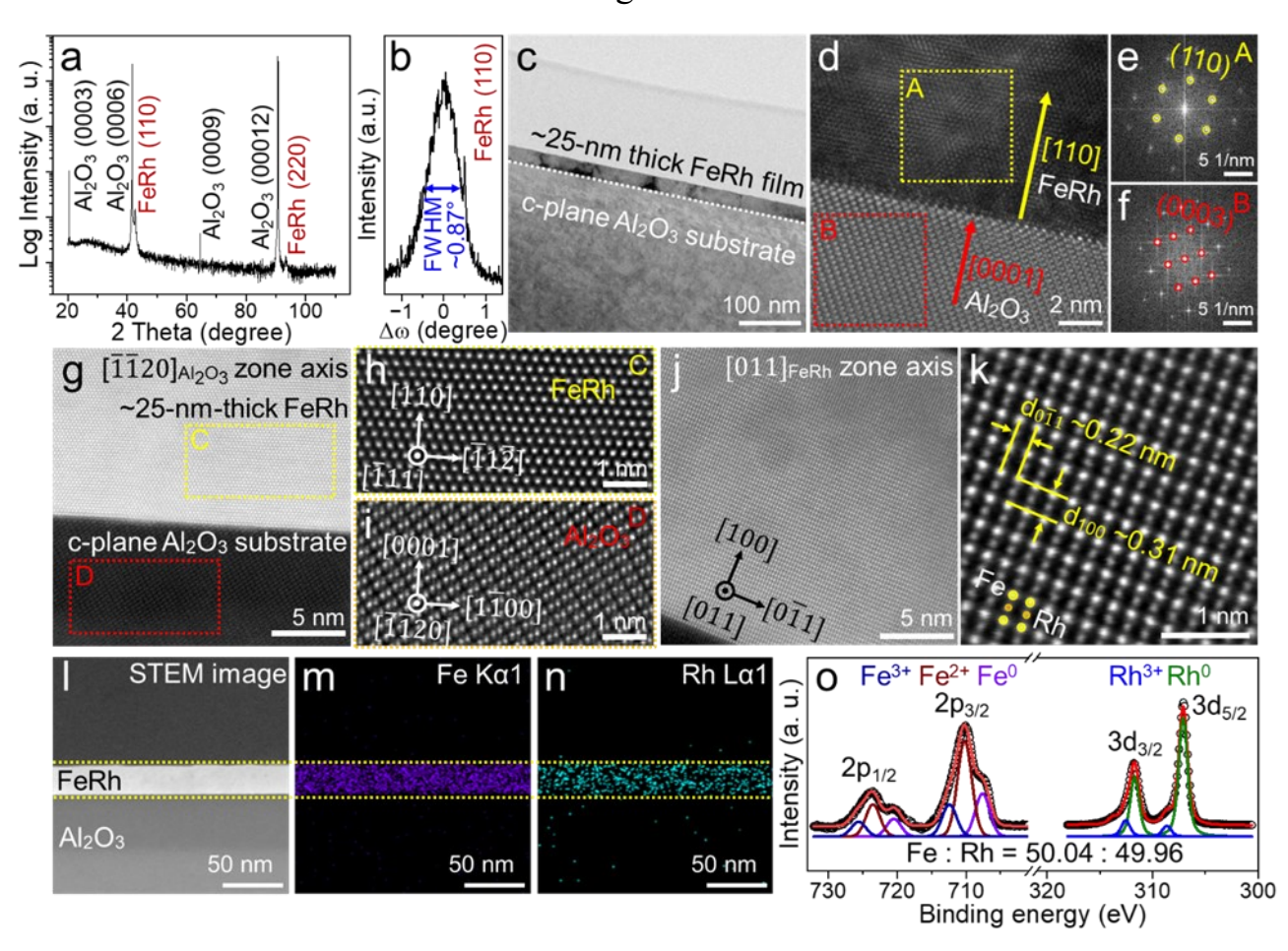


Figure 2

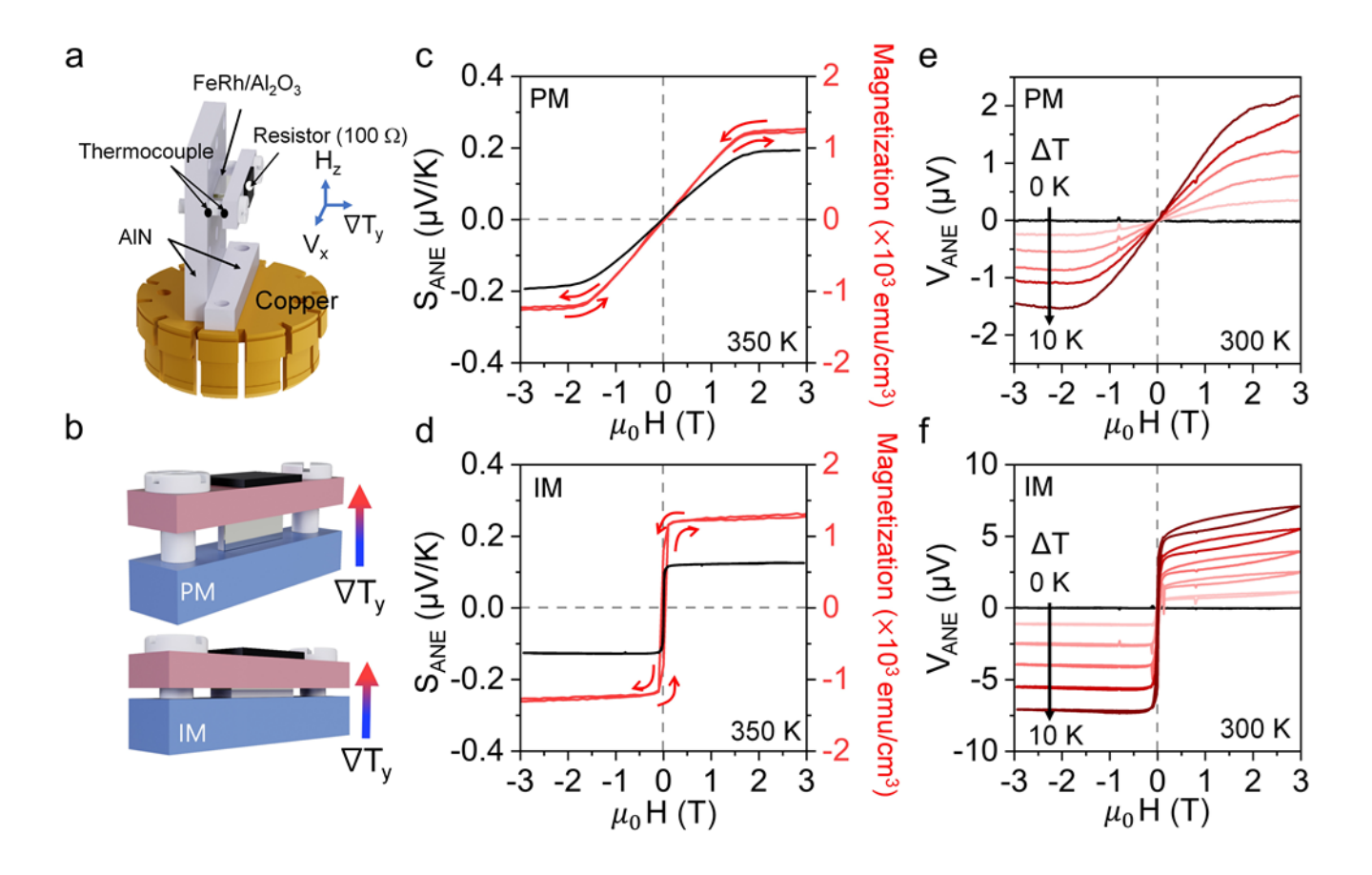


Figure 3

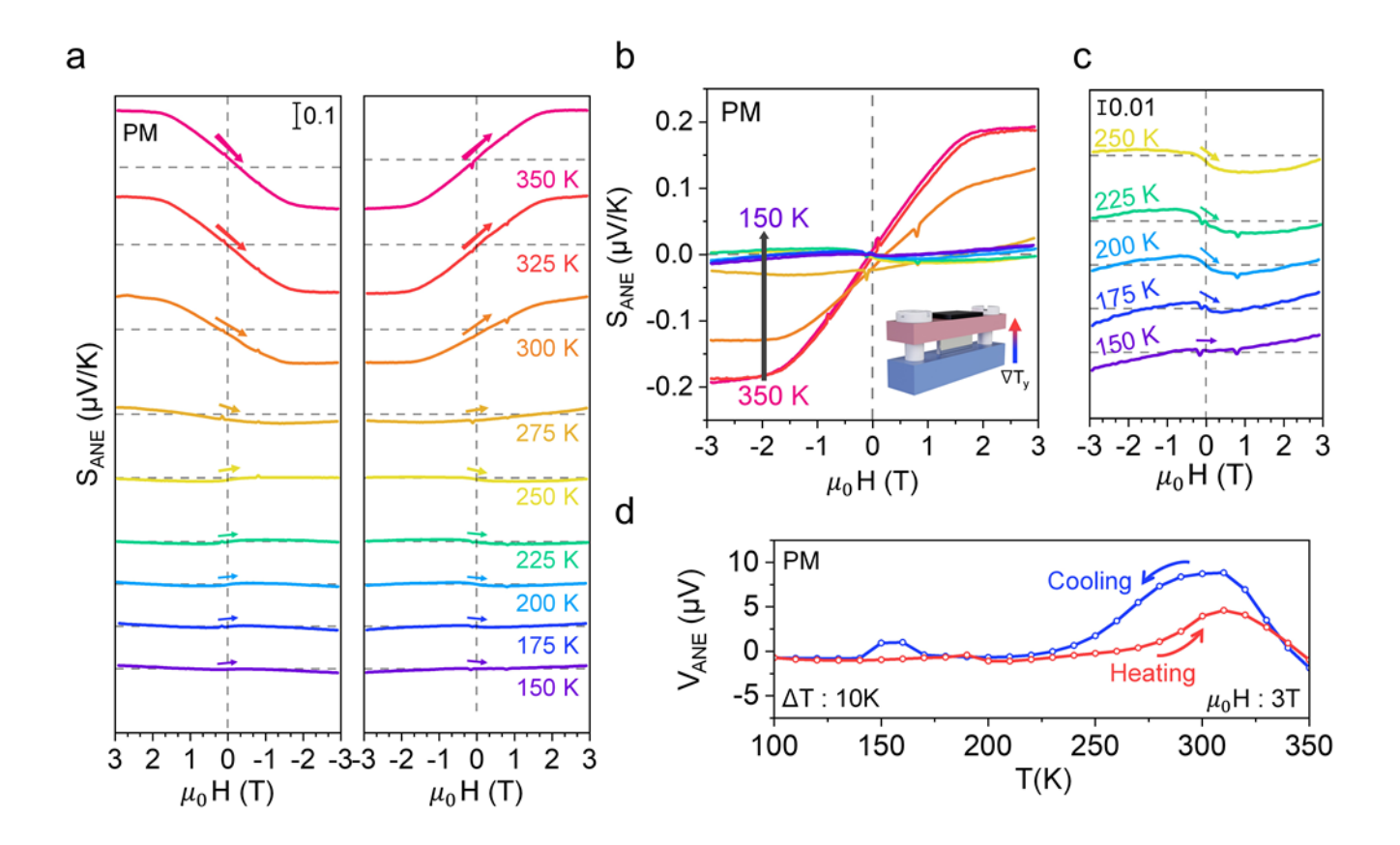


Figure 4

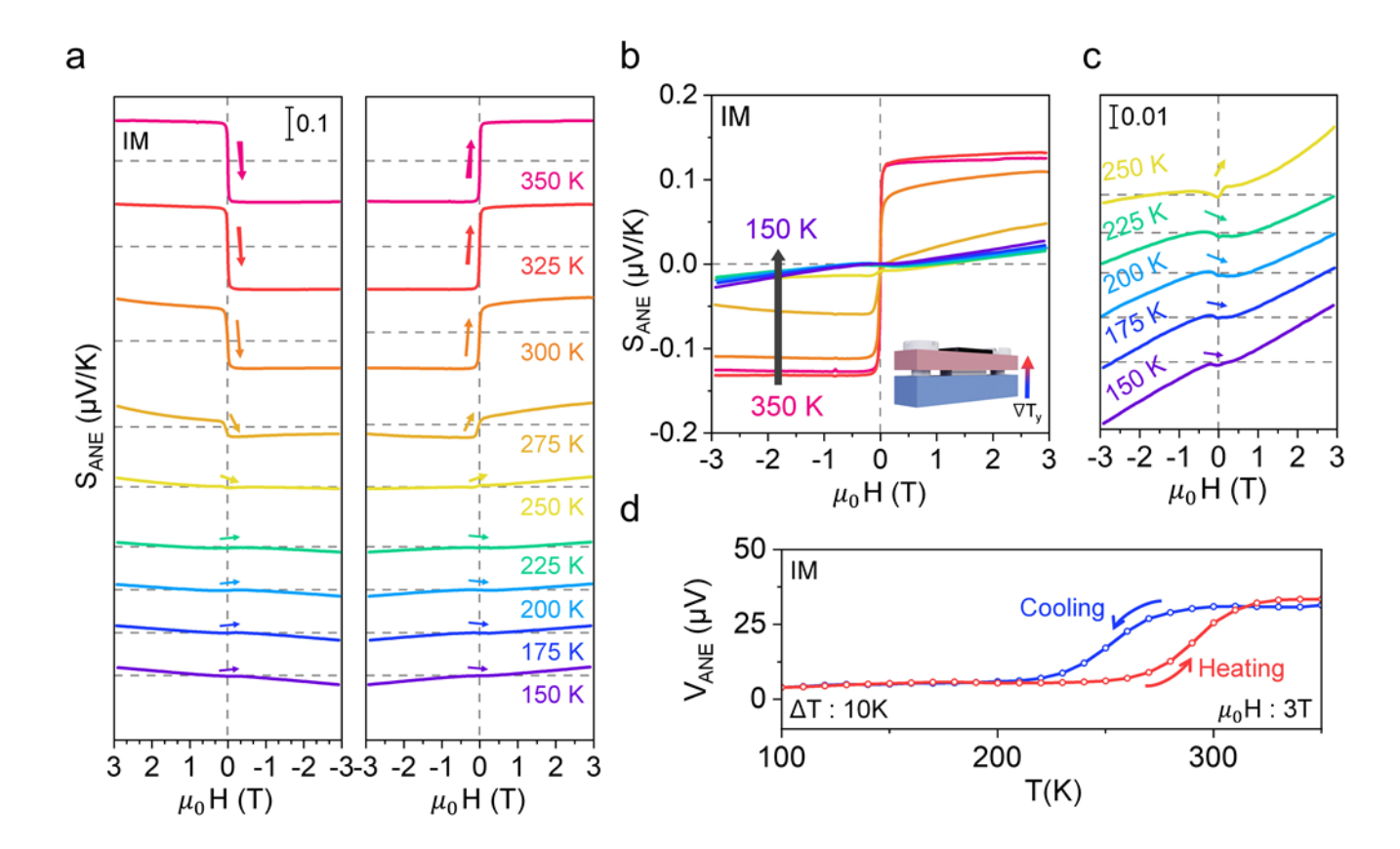


Figure 5

